
DYNAMIC MIXED TURBULENCE MODELING USING A SUPER-RESOLUTION GENERATIVE ADVERSARIAL APPROACH

L. Nista¹, C. D. K. Schumann², T. Grenga³, J. F. MacArt⁴, A. Attili⁵, and H. Pitsch¹

¹Institute for Combustion Technology, RWTH Aachen University, Aachen, 52056, Germany

²Department of Engineering, University of Cambridge, Cambridge, CB2 1PZ, United Kingdom

³Department of Aeronautics and Astronautics, Faculty of Engineering and Physical Sciences, University of Southampton, Southampton, SO17 1BJ, United Kingdom

⁴Department of Aerospace and Mechanical Engineering, University of Notre Dame, Notre Dame, IN 46556, USA

⁵School of Engineering, Institute for Multiscale Thermofluids, University of Edinburgh, Edinburgh, EH9 3FD, United Kingdom

ABSTRACT

A dynamic mixed super-resolution model (DMSRM) for large-eddy simulations (LESs) is proposed, which combines the traditional dynamic mixed model (DMM) formulation with the generation of super-resolved velocity fields from which the subfilter-scale (SFS) stress tensor can be computed. A data-driven super-resolution generative adversarial network (SR-GAN) is employed to upsample the grid-filtered velocity fields by a factor of two, enabling the evaluation of both scale-similarity and the dynamic Smagorinsky contributions. *A priori* analyses of forced homogeneous isotropic turbulence show that the SR-GAN accurately reconstructs fine-scale flow features and generalizes well across different filter sizes and higher Reynolds number flow configurations, even for unseen input fields. The DMSRM reproduces SFS stresses and energy dissipation more accurately than the traditional DMM. *A posteriori* LES calculations further confirm that DMSRM predicts the energy spectrum and intermittency more accurately than DMM, even for different LES grid-scale resolutions and for higher Reynolds numbers than those used for training. Unlike DMM, DMSRM yields realistic backscatter and physically consistent SFS energy dissipation. These improvements arise from the physically accurate super-resolved fields generated by the SR-GAN, from which SFS stresses are directly computed. The result is a closure that accurately reproduces stress magnitudes and dissipation while reducing reliance on additional dissipation from the dynamic term. The DMSRM formulation achieves a balance of physical fidelity, robustness, and computational efficiency, offering a promising alternative to traditional DMMs for turbulence LES modeling.

1 Introduction

Direct numerical simulation (DNS) resolves all time and length scales of turbulent flows but faces prohibitive computational costs for engineering applications. To address this, large-eddy simulation (LES) solves spatially filtered equations, resulting in significant cost reduction [1, 2]. The LES flow field is decomposed into resolved and subfilter-scale (SFS) components, and the filtered governing equations are solved with the SFS terms requiring closure. Accurate closure models are therefore essential for capturing the subfilter-scale influence on the resolved scales [3]. While we focus on models for the SFS stress tensor, analogous challenges exist for other SFS terms, especially when reacting flows are considered [4].

Various approaches have been proposed to model the SFS contributions in incompressible flows, which are broadly classified into functional and structural models. Functional models, such as the widely used dynamic Smagorinsky model (DSM) [5], capture the mean dissipative effect of SFS motions on the resolved scales, often through an eddy-viscosity formulation. However, correctly predicting the mean dissipation might be insufficient to reproduce the

correct flow statistics, and *a priori* analyses demonstrated that the DSM's modeled and exact SFS stress tensors do not correlate well [6]. Conversely, structural models, such as the original scale-similarity model (SSM) [7], aim to improve the fidelity of SFS stress tensors by leveraging the assumption of scale similarity. The velocity field at scales below LES grid resolution is postulated to be similar to that at scales above, and an additional test filter is applied at the resolved scale to capture the structural characteristics of SFS turbulence [8]. *A priori* studies have shown that the stresses modeled with the SSM are more similar to the exact SFS stress than those with the DSM; however, they generally do not provide sufficient dissipation *a posteriori*, which can lead to numerical instability.

A straightforward approach for developing closure models that simultaneously possesses (a) favorable structural properties, and (b) enough mean energy dissipation, is to combine functional and structural models into the so-called dynamic mixed models (DMMs) [9]. In DMMs, the structural scale-similarity component provides an accurate representation of the SFS stress tensor, while the functional dissipative component ensures stability [3].

Since the physical accuracy of DMMs strongly depends on the fidelity of the scale-similarity contribution, several improvements to the original SSM formulation have been proposed, specifically regarding the choices for the test filter kernel and width, and the number of dynamic model coefficients [10–12]. Additionally, a number of approaches have been proposed as alternatives to traditional similarity-based models, which postulate a representation of the SFS velocity field, from which the SFS stresses can be reconstructed. These methods differ in complexity and cost, often introducing additional assumptions or requiring auxiliary equations. For example, Scotti *et al.* [13] proposed a method based on fractal representations of turbulence. This model is computationally inexpensive but neglects the local flow dynamics and requires an additional transport equation. McDonough *et al.* [14] introduced a chaotic map model that mimics turbulent fluctuations via a low-dimensional chaotic dynamical system. Though simple and efficient, this method requires the specification of a suitable dynamic, which is non-trivial for complex flows. An approach proposed by Domaradzki *et al.* [15] involves explicit computation of SFS fluctuations by solving a simplified advection equation. This technique is cost-effective but requires an approximate inverse filter, which is challenging to specify [3]. More recently, data-driven deep learning (DL) approaches have also been explored, particularly through super-resolution (SR) frameworks. Low-resolution (LR) LES fields are upsampled to high-resolution (HR) representations on finer meshes using data-driven SR frameworks, which recover unresolved flow features by learning multi-scale structures and intermittency directly from high-fidelity data [16, 17]. In particular, generative convolutional models such as generative adversarial networks (GANs) have demonstrated DNS-level fidelity in *a priori* tests, strong generalization to unseen flow conditions, and significantly better accuracy than traditional algebraic models [17–20].

While *a priori* tests have shown remarkable model-fitting capabilities across different flow conditions, *a posteriori* LES with data-driven SR closure models (SR-LES) remain scarce, especially for large upsampling factors, i.e., for large LES-to-DNS filter ratios, and high Reynolds number flows. This limitation arises because the cost of training and evaluating SR models scales with the upsampling factor and is driven by the increased training dataset size, complexity of learning, and number of trainable parameters. Even more importantly, the memory and inference time requirements of DNS-level SR pose significant barriers to scalability [21]. Furthermore, SR-LES imposes restrictions on domain decomposition due to convolutional boundary effects, which limit parallel scalability and increase computational cost [22]. As a result, employing SR-LES for full-scale (DNS-like) SFS reconstruction is impractical even for moderate Reynolds number flows.

Nevertheless, SR-based methods may remain promising for SFS modeling when combined with existing LES model formulations. A known limitation of scale similarity and mixed models is that the SFS stress tensor is derived from the grid-filtered velocity field, which is typically numerically inaccurate. In addition, a test filter is usually applied, which can further increase errors. Even if the grid-filtered velocity field is considered physically accurate, the arbitrary choice of test filter kernel and size may reduce model fidelity. In contrast, SR-GANs leverage high-fidelity DNS data and physics-informed adversarial training to generate super-resolved velocity fields that are consistent with actual turbulence dynamics [20]; these fields are then used to evaluate the SFS terms, potentially improving predictive accuracy even when applied to imperfect grid-filtered velocity fields.

Based on the potential advantages outlined above, we introduce a dynamic mixed SR-based model (DMSRM) (Section 2) that combines (a) the robustness and computational efficiency of DMMs, (b) SR-generated velocity fields for scale-similarity-based SFS stress computation, and (c) the physically consistent SR reconstruction capabilities of SR-GANs. By leveraging SR-GANs (Section 4), the proposed formulation avoids arbitrary test filters by explicitly reconstructing super-resolved velocity fields at a slightly increased resolution compared to the LES grid. This enables the use of a scale-similarity-like formulation with a modest upsampling ratio of two, thereby avoiding the computational cost of conventional SR-based approaches. We evaluate the DMSRM using two forced homogeneous isotropic turbulence (HIT) datasets (Section 3), examining both its *a priori* (Section 5) and *a posteriori* (Section 6) performance with various training filter kernels, filter sizes, and flow conditions. Additionally, we assess the model's numerical stability and the individual contributions of its components (Section 6.2), as well as its computational efficiency rel-

ative to the standard DMM (Section 7). The overarching objective is to develop a hybrid modeling framework that leverages the capabilities of DL-based SR frameworks while maintaining feasible computational cost and preserving the stability and efficiency of DMMs.

2 LES formulation and dynamic mixed models

The filtered momentum equation for incompressible flow is

$$\frac{\partial \bar{u}_j}{\partial t} + \frac{\partial(\bar{u}_i \bar{u}_j)}{\partial x_i} = -\frac{1}{\rho} \frac{\partial \bar{p}}{\partial x_j} + \nu \frac{\partial^2 \bar{u}_j}{\partial x_i \partial x_i} - \frac{\partial \tau_{ij}}{\partial x_i} + \bar{f}_j \text{ with } j = 1, 2, 3, \quad (1)$$

where \bar{u}_j are the LES-filtered velocity components, the filtered pressure field \bar{p} includes the isotropic part of the SFS stress tensor, ρ is the density, ν is the kinematic viscosity, and \bar{f}_j is a volumetric forcing term (see Section 3). We consider grid LES-filtered solutions of (1) represented on a discrete LES domain $\bar{\Omega} \in \mathbb{R}^{\bar{N}_x \times \bar{N}_y \times \bar{N}_z}$, where \bar{N}_i is the number of LES grid points in the i^{th} direction, and $\bar{\Delta}$ is the uniform LES grid spacing. In (1), the deviatoric SFS stress tensor is

$$\tau_{ij} = \tau_{ij}^R - \frac{2}{3} k_r \delta_{ij}, \quad \text{with } \tau_{ij}^R = \bar{u}_i \bar{u}_j - \bar{u}_i \bar{u}_j \quad \text{and } k_r \equiv \frac{1}{2} \tau_{ii}^R, \quad (2)$$

where τ_{ij}^R is the SFS stress tensor and k_r is the residual kinetic energy.

2.1 Dynamic Smagorinsky model

The (dynamic) Smagorinsky model for τ_{ij} is

$$\tau_{ij}^{\text{DSM}} = -2(C_s \bar{\Delta})^2 |\bar{S}| \bar{S}_{ij}, \quad (3)$$

where in the dynamic variant, the coefficient C_s^2 is computed using the procedure of Germano *et al.* [5]. To ensure numerical stability, spatial averaging is applied to the dynamically computed coefficient as proposed by Lilly [23]. In (3), the filtered strain-rate tensor \bar{S}_{ij} and its magnitude $|\bar{S}|$ are

$$\bar{S}_{ij} = \frac{1}{2} \left(\frac{\partial \bar{u}_i}{\partial x_j} + \frac{\partial \bar{u}_j}{\partial x_i} \right), \quad |\bar{S}| = (\bar{S}_{ij} \bar{S}_{ij})^{1/2}. \quad (4)$$

The dynamic procedure operates by applying a low-pass *test filter* of width $2\bar{\Delta}$ to the velocity field and invoking the scale-similarity hypothesis over the inter-scale range (i.e., for scales between $\bar{\Delta}$ and $2\bar{\Delta}$). The dynamic Smagorinsky model is a component of both the dynamic mixed model and our proposed dynamic mixed super-resolution-based model, though their inter-scale ranges are different. We discuss these two models in the subsequent subsections.

2.2 Dynamic mixed model

The dynamic mixed model combines the dynamic Smagorinsky model and the scale-similarity model as

$$\tau_{ij}^{\text{DMM}} = \tau_{ij}^{\text{DSM}} + \tau_{ij}^{\text{SSM}} = \underbrace{-2(C_d \bar{\Delta})^2 |\bar{S}| \bar{S}_{ij}}_{\text{DSM} \rightarrow \text{DMM}} + \underbrace{C_L \tau_{ij}^{\text{SSM}}}_{\text{SSM}}, \quad (5)$$

where the scale-similarity coefficient is $C_L = 1$, and a dynamic procedure is applied to obtain C_d^2 ([10]; see Appendix B). Here, the DSM contribution to the DMM is denoted “DSM → DMM.” The scale-similarity term is

$$\tau_{ij}^{\text{SSM}} = \widehat{\bar{u}_i \bar{u}_j} - \widehat{\bar{u}_i} \widehat{\bar{u}_j}, \quad (6)$$

where $\widehat{\cdot}$ is the test-filter operator—here, a spectral filter with kernel width $2\bar{\Delta}$ (see table 1 and Appendix A).

In constructing (5), the single-parameter dynamic formulation is preferred over the two-parameter approach, as the two-parameter dynamic procedure tends to heavily favor the scale-similarity contribution due to its higher correlation with the DNS-evaluated SFS stress. This often results in a model that is insufficiently dissipative. The dynamic coefficients can be decoupled [24], but this increases computational cost and is not considered here. The definition of the SSM in Eq. (6) is based on the improved version of Sarghini *et al.* [25] compared to the original implementation proposed by Bardina [7]. An overview of the various DMM formulations is provided in [3, 6] for different filter kernels, filter sizes, and different dynamic coefficient evaluation methods.

2.3 Dynamic mixed SR-based model

The dynamic mixed super-resolution-based model is similar in spirit to the dynamic mixed model but has one principal difference: rather than evaluating the scale-similarity term and dynamic Smagorinsky contribution for scales coarser than the LES grid, it instead evaluates them on finer scales, i.e., for the energy content between the LES grid-scale solution and its super-resolved counterpart.

Let u_i^* be a super-resolved velocity field on an auxiliary mesh $\Omega^* \in \mathbb{R}^{2\bar{N}_x \times 2\bar{N}_y \times 2\bar{N}_z}$ obtained by upsampling \bar{u}_i using an SR-GAN model (see Section 4), and let $\Delta^* = \bar{\Delta}/2$ be the uniform mesh spacing on Ω^* . While we use an upsampling ratio of two to minimize computational cost and memory requirements, in principle, any upsampling ratio of the form 2^n , where $n \in \mathbb{N}$ is the number of upsampling layers (see Section 4), could be used. In the DMSRM context, we use $\widehat{\cdot}$ to denote a spectral filter kernel of width $2\Delta^* = \bar{\Delta}$ (i.e., filtering SR-scale fields to the LES-grid scale) and $\widetilde{\cdot}$ to denote a spectral filter kernel of width $4\Delta^* = 2\bar{\Delta}$ (i.e., filtering SR-scale fields to twice the LES-grid scale). We also use \cdot to denote a discrete downsampling operator to restrict Ω^* fields to $\bar{\Omega}$. Table 1 summarizes these operators and the domains on which they operate.

Quantity	Description	Defined on
\bar{u}_i	Velocity field at (LES) grid-filter scale	$\bar{\Omega}$
\bar{Q}	Quantity evaluated using \bar{u}_i	$\bar{\Omega}$
u_i^*	SR-GAN reconstructed velocity field from \bar{u}_i	Ω^*
Q^*	Quantity evaluated using u_i^*	Ω^*

Operator (model)	Filter kernel	Mapping
$\widehat{\cdot}$ (DMM)	Spectral, $2\bar{\Delta}$	$\bar{\Omega} \rightarrow \bar{\Omega}$
$\widetilde{\cdot}$ (DMM)	Spectral, $4\bar{\Delta}$	$\bar{\Omega} \rightarrow \bar{\Omega}$
$\widehat{\cdot}$ (DMSRM)	Spectral, $2\Delta^* = \bar{\Delta}$	$\Omega^* \rightarrow \Omega^*$
$\widetilde{\cdot}$ (DMSRM)	Spectral, $4\Delta^* = 2\bar{\Delta}$	$\Omega^* \rightarrow \Omega^*$
\cdot (DMSRM)	– (Downsampling)	$\Omega^* \rightarrow \bar{\Omega}$ (factor: 2)

Table 1: Overview of quantities, notations, and operators employed by the DMSRM or DMM. The “defined on” column indicates the discrete domain at which each quantity is defined, where $\bar{\Omega}$ and Ω^* indicate the discrete LES and super-resolved domains, respectively. For operators, the “mapping” column specifies the input and output domains for each operator. The definition of the spectral filter kernel and the downsampling operator are reported in Appendix A.

The DMSRM then employs a SR-scale term

$$\tau_{ij}^* = -2C_d^2(\Delta^*)^2|S^*|S_{ij}^* + (\widehat{u}_i^* \widehat{u}_j^* - \widetilde{u}_i^* \widetilde{u}_j^*), \quad (7)$$

where S_{ij}^* is the SR-scale strain-rate tensor with magnitude $|S^*| = (2S_{ij}^* S_{ij}^*)^{1/2}$, as well as a “test-filtered SR-scale” (i.e., LES-scale) term

$$T_{ij} = -2C_d^2(2\Delta^*)^2|\widehat{S}^*|\widehat{S}_{ij}^* + (\widetilde{\widehat{u}}_i^* \widetilde{\widehat{u}}_j^* - \widetilde{\widetilde{u}}_i^* \widetilde{\widetilde{u}}_j^*), \quad (8)$$

that is needed to evaluate C_d^2 dynamically. It is important to note that both (7) and (8) are evaluated on Ω^* . At the SR scale, the Germano identity [5] is

$$\mathcal{L}_{ij} = (\widehat{u}_i^* \widehat{u}_j^* - \widetilde{u}_i^* \widetilde{u}_j^*) = T_{ij} - \tau_{ij}^*. \quad (9)$$

Substituting (7) and (8) into (9) yields

$$\begin{aligned} \mathcal{L}_{ij} &= C_d^2 \mathcal{M}_{ij} + \mathcal{N}_{ij}, \\ \mathcal{M}_{ij} &= -2(\Delta^*)^2(4|\widehat{S}^*|\widehat{S}_{ij}^* - |\widehat{S}^*|\widehat{S}_{ij}^*), \\ \mathcal{N}_{ij} &= (\widetilde{\widehat{u}}_i^* \widetilde{\widehat{u}}_j^* - \widetilde{\widetilde{u}}_i^* \widetilde{\widetilde{u}}_j^*) - (\widehat{u}_i^* \widehat{u}_j^* - \widetilde{u}_i^* \widetilde{u}_j^*). \end{aligned} \quad (10)$$

The model coefficient C_d^2 is evaluated dynamically as

$$C_d^2 = \frac{\langle \mathcal{L}_{ij} \mathcal{M}_{ij} \rangle - \langle \mathcal{N}_{ij} \mathcal{M}_{ij} \rangle}{2\langle \mathcal{M}_{ij} \mathcal{M}_{ij} \rangle}, \quad (11)$$

where $\langle \cdot \rangle$ denotes averaging in homogeneous directions to prevent numerical instabilities. The dynamic coefficient evaluation corresponds to minimizing the DMSRM modeling error

$$\begin{aligned}\mathcal{E}_{ij} = & \langle \mathcal{L}_{ij} \mathcal{L}_{ij} \rangle + (C_d^2)^2 \langle \mathcal{M}_{ij} \mathcal{M}_{ij} \rangle + \langle \mathcal{N}_{ij} \mathcal{N}_{ij} \rangle \\ & - 2(C_d^2 \langle \mathcal{L}_{ij} \mathcal{M}_{ij} \rangle + \langle \mathcal{L}_{ij} \mathcal{N}_{ij} \rangle - C_d^2 \langle \mathcal{N}_{ij} \mathcal{M}_{ij} \rangle).\end{aligned}$$

Finally, the DMSRM for the subfilter stress is obtained by filtering (7) to the LES grid scale and downsampling to $\bar{\Omega}$:

$$\tau_{ij}^{\text{DMSRM}} = \underbrace{-2C_d^2(\Delta^*)^2 |S^*| \widehat{S}_{ij}^*}_{\text{DSM} \rightarrow \text{DMSRM}} + \underbrace{(\widehat{\overline{u}_i^* u_j^*} - \widehat{\overline{u}_i^*} \widehat{\overline{u}_j^*})}_{\text{SRM}}. \quad (12)$$

Here, the first term is the DSM contribution to the DMSRM, denoted “DSM \rightarrow DMSRM,” and the second term denotes the *super-resolution model* (SRM) contribution.

3 DNS datasets, preprocessing, and LES setup

In this work, DNS data of forced HIT is employed as it is a canonical configuration with well-characterized turbulence statistics and no boundary effects. These properties make it an established benchmark for evaluating turbulence closure models before extending them to more complex flows.

We consider two forced HIT DNS datasets. The Taylor-microscale Reynolds numbers of the two DNSs are $Re_\lambda \approx 110$ and $Re_\lambda \approx 200$. These datasets are denoted as Re110 and Re200, respectively. Both simulations are performed on a triply periodic domain of size $L = 2\pi$ in each direction, which is uniformly discretized using 256^3 points for Re110 and 512^3 points for Re200. These grids satisfy $dx/\eta \leq 2$, where dx is the uniform grid spacing and η is the Kolmogorov length scale. The same configurations are also employed for *a posteriori* LES analyses and verification.

The simulations are performed using the CIAO code [26], which uses a staggered grid for the velocity components, with mass continuity enforced by solving a Poisson equation for the hydrodynamic pressure using preconditioned multigrid methods. The second-order Crank–Nicolson scheme is used for time advancement, and a fourth-order finite-difference scheme is applied for spatial discretization. Independent of whether the LES or DNS approach is considered, a sharp-spectral forcing with a cut-off wavenumber of $\kappa_c = 3$ is applied, similar to the setup employed by Eswaran *et al.* [27]. The DNS data are publicly available [28], and their parameters are reported in table 2.

Dataset	L	N	Re_λ	dx/η	L/ℓ	Train	Test
Re110	2π	256^3	110	1.58	5.26	•	
Re200	2π	512^3	200	1.61	5.26	•	•

Table 2: Simulation parameters for each DNS dataset. “ L ” indicates the physical size of the periodic computational domain in each direction, N is the number of mesh points, Re_λ is the Taylor-microscale Reynolds number, dx/η is the mesh resolution relative to the Kolmogorov microscale η , and L/ℓ is the ratio of the domain size to the integral scale ℓ . “Train” and “Test” flags indicate which data were used in SR-GAN training and *a priori* and *a posteriori* testing, respectively.

To train the SR-GAN framework, 1400 snapshots of the three-dimensional velocity vector are collected from the Re110 and Re200 datasets. The snapshots are taken after an initial transient period of $t \approx 5\tau_0$, where τ_0 is the eddy-turnover time, with two snapshots extracted every τ_0 . Unlike conventional SR approaches that aim to directly reconstruct DNS-scale resolution, the SR-GAN framework in this work is trained to upsample to an intermediate resolution between filtered-DNS (F-DNS) fields, which are obtained using different filter widths. The input and target training pair consists of the following pairs of fields.

- The low-resolution input fields, denoted “ ϕ_{LR} ,” are obtained by filtering DNS snapshots with box, Gaussian, and spectral filter kernels using a filter width $\Delta_{\text{LR}} = n_{\Delta_{\text{LR}}} dx$. Here, $n_{\Delta_{\text{LR}}}$ specifies the LR filter size. Each F-DNS is then discretely downsampled by a factor of $n_{\Delta_{\text{LR}}}$ to produce the F-DNS field on a coarser grid, independent of the filter kernel applied. The definition of the filter kernels along with the downsampling operator is given in Appendix A. The filter kernel to obtain ϕ_{LR} is randomly selected during training to prevent the generator from learning an explicit inverse of the filters, as observed by Nista *et al.* [20];
- The corresponding high-resolution target fields, denoted “ ϕ_{HR} ,” are obtained from spectrally filtered DNS data using a smaller filter width $\Delta_{\text{HR}} = n_{\Delta_{\text{HR}}} dx$. Given the fixed upsampling ratio of the SR-GAN framework, the HR filter size is $n_{\Delta_{\text{HR}}} = n_{\Delta_{\text{LR}}}/2$.

Of the total number of extracted snapshots, 80% are used for the training dataset, while the remaining 20% are randomly divided between validation and testing. Four different training configurations are employed for the SR-GAN framework, and their performance is compared through *a priori* and *a posteriori* investigations.

4 Generative adversarial framework and training strategies

Figure 1 shows the *SimilarityGAN* SR-GAN framework [20, 22] used in this work. *SimilarityGAN* is designed for turbulence SR reconstruction and employs an adversarial training strategy using distinct generator and discriminator neural networks. This enables supervised, semisupervised, and fully unsupervised learning without relying on user-defined objective functions [29]. In GAN-based SR, the generator produces an SR version of ϕ_{LR} , denoted ϕ_{SR} , while the discriminator network attempts to distinguish between ϕ_{SR} and ϕ_{HR} . Throughout the training, the generator progressively learns to produce fields that are indistinguishable from ϕ_{HR} . In turn, the discriminator learns to judge the authenticity of the samples. It should be noted that the DMSRM formulation is agnostic to the specific SR framework employed. *SimilarityGAN* is selected here due to its strong reconstruction performance compared to traditional fully supervised SR-based architectures for turbulent flow reconstruction [20].

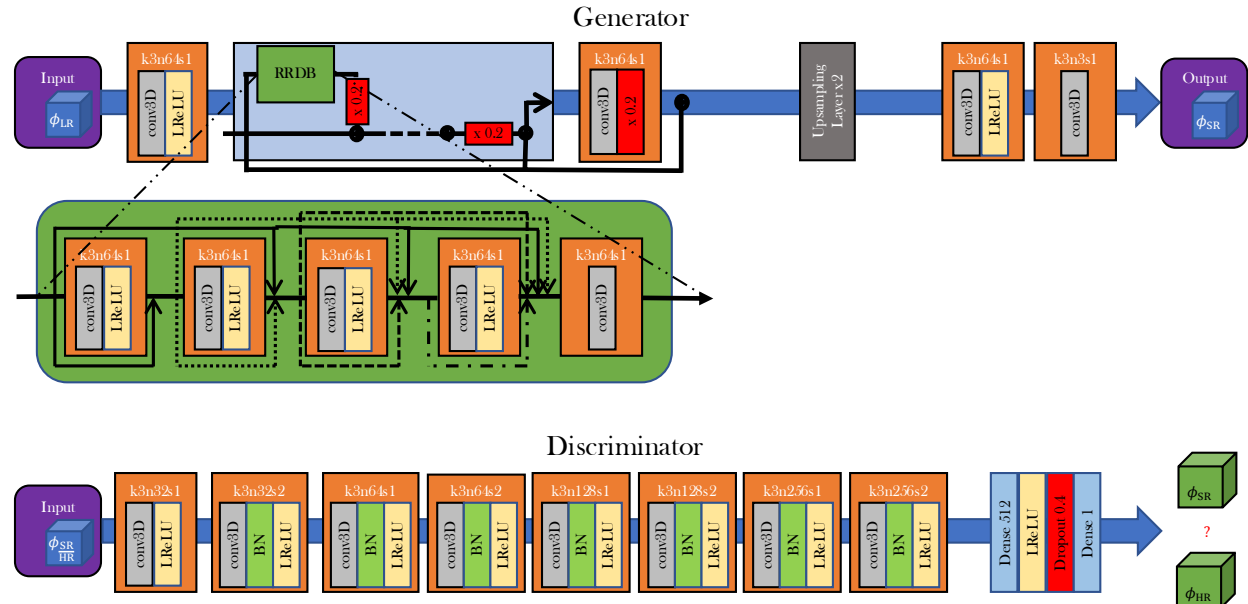


Figure 1: The generator (above) and discriminator (below) structures of the *similarityGAN* framework. In these illustrations, ϕ_{LR} denotes the LR input field, ϕ_{SR} denotes the SR output field, and ϕ_{HR} denotes the corresponding HR target field. Each convolutional block contains kernels of size k , n filter maps, and s strides along each spatial dimension of the convolutional layer.

The generator, shown in the upper row of figure 1, is a CNN-based architecture that produces the u_i^* field used by the DMSRM given the \bar{u}_i input. Inspired by the work of Wang *et al.* [30], the residual-in-residual dense block (RRDB) is used in this architecture, which comprises skip connections and three-dimensional convolution layers, which allow for efficient feature learning and extraction of small-scale features. The upsampling operation is performed close to the network’s output so that feature extraction and refinement occur at the LR scale, which minimizes computational cost and memory requirements. As demonstrated by Ledig *et al.* [31], this design also ensures that the generator focuses on learning rich hierarchical representations before the spatial resolution is increased, therefore improving fidelity and training stability. The upsampling layer in the generator increases the spatial resolution by a factor of two in each dimension using nearest-neighbor interpolation, followed by a convolution operation to refine the output. The generator contains approximately 11 million trainable parameters.

The discriminator, shown in the lower row of figure 1, is structured as a deep deconvolutional framework comprising fully connected layers, including convolutional layers and leaky rectified linear activation (LReLU) activation functions similar to the generator but with a binary classification output. The discriminator has a depth comparable to that of the generator with approximately 15 million trainable parameters, ensuring balanced complexity during adversarial

training. This discriminator structure facilitates efficient adversarial training and preserves its ability to discriminate between ϕ_{HR} and ϕ_{SR} [20].

4.1 Training strategies

SR-GAN training proceeds in three stages: (1) independent, fully-supervised training of the generator (pretraining), (2) semi-supervised training of the SR-GAN, and (3) partially unsupervised training of the SR-GAN. These stages are explained below. The pretraining stage is discussed after the semi-supervised training stage.

During the semi-supervised training, the generator’s loss function (\mathcal{L}_{GEN}) is comprised of four contributions: a pixel-wise reconstruction loss (L_{pixel}), a gradient-based loss to enforce small-scale fidelity (L_{gradient}), a physics-based continuity loss ($L_{\text{continuity}}$), and an adversarial loss ($L_{\text{adversarial}}$),

$$\begin{aligned}\mathcal{L}_{\text{GEN}} &= \alpha_1 L_{\text{pixel}} + \alpha_2 L_{\text{gradient}} + \alpha_3 L_{\text{continuity}} + \alpha_4 L_{\text{adversarial}} \\ L_{\text{pixel}} &= \text{MSE}(\phi_{\text{SR}}, \phi_{\text{HR}}) \\ L_{\text{gradient}} &= \text{MSE}(\nabla \phi_{\text{SR}}, \nabla \phi_{\text{HR}}) \\ L_{\text{continuity}} &= \text{MSE}(\nabla \cdot \phi_{\text{SR}}, 0) \\ L_{\text{adversarial}} &= -\mathbb{E}[\log(\sigma(D(G(\phi_{\text{LR}})) - \mathbb{E}[D(\phi_{\text{HR}})]))] \\ &\quad - \mathbb{E}[\log(1 - \sigma(D(\phi_{\text{HR}}) - \mathbb{E}[D(G(\phi_{\text{LR}}))]))],\end{aligned}\tag{13}$$

where $\mathbb{E}[\cdot]$ denotes the expectation over the training mini-batch, $\sigma(\cdot)$ is the sigmoid activation function, and D and G represent the discriminator’s and generator’s operators, respectively. The weighting coefficients are $\alpha_i = [0.88994, 0.06, 0.05, 6 \cdot 10^{-5}]$; these were chosen through hyperparameter tuning, such that the absolute value of each term in \mathcal{L}_{GEN} is of the same order during the semi-supervised training [20]. The weighting of these coefficients is appropriate for the forced HIT datasets employed in this work, but may require adjustment for other flow configurations. All mean-squared error (MSE) terms are evaluated element-wise. The adversarial loss is based on the relativistic average GAN (RaGAN) definition [32], given its improved stability performance over the traditional adversarial loss. The discriminator is trained using the corresponding RaGAN-based loss,

$$\begin{aligned}\mathcal{L}_{\text{DISC}} &= \mathbb{E}[\log(\sigma(D(\phi_{\text{HR}}) - \mathbb{E}[D(G(\phi_{\text{LR}}))]))] \\ &\quad + \mathbb{E}[\log(1 - \sigma(D(G(\phi_{\text{LR}}) - \mathbb{E}[D(\phi_{\text{HR}})])))].\end{aligned}\tag{14}$$

The first term in Eq. (14) encourages the discriminator to assign higher fidelity scores to ϕ_{HR} relative to the average score of ϕ_{SR} , while the second term penalizes the discriminator if the ϕ_{SR} are rated more realistic than the average ϕ_{HR} , unless they closely resemble physically realistic data.

Due to the well-known training instabilities associated with SR-GAN frameworks, an independent, fully supervised pretraining of the generator is employed before the semi-supervised SR-GAN training phase. In the pretraining phase, the generator is trained to minimize L_{pixel} , L_{gradient} , and $L_{\text{continuity}}$. This means that the discriminator is not employed during this initial training phase. The generator is randomly initialized to avoid undue bias. This pretraining stage provides a well-conditioned and physically consistent starting point for the subsequent training phases.

Recent studies have emphasized the critical role of the initial learning rate for local convergence and stability of SR-GAN training. Accordingly, learning rate choices for both the generator and discriminator follow recent recommendations shown to enhance GAN stability in turbulent flow contexts. The generator is pretrained with an initial learning rate of 1×10^{-4} , while the discriminator is initialized with a lower initial learning rate of 5×10^{-5} to prevent its dominance over the generator, consistent with strategies reported by Mescheder *et al.* [33] and Nista *et al.* [34]. Both networks are optimized using the ADAM algorithm with no learning rate schedule applied [35].

By training the discriminator to distinguish ϕ_{HR} and ϕ_{SR} during the semi-supervised training phase, physical information is implicitly embedded within its latent representation. As a result, the discriminator functions as a physics-informed loss component and guides the generator through adversarial feedback toward producing physically plausible ϕ_{SR} . This mechanism is further leveraged in a third training phase known as partially unsupervised training (PUT), introduced by Nista *et al.* [20]. In the PUT phase, LES of forced HIT are performed using the same numerical solver described in Section 3, but on coarser grids consistent with the chosen $n_{\Delta_{\text{LR}}}$ used to generate the ϕ_{LR} . In these LES calculations, the unresolved scales are either closed using the DSM (Eq. (3)), the DMM (Eq. (5)), or their influence is not modeled (“implicitly modeled” LES). These closure models are chosen due to their widespread adoption, though the framework is not limited to their use.

When multiple $n_{\Delta_{\text{LR}}}$ are employed in the training setup, as is further described in Section 4.2, LES calculations are performed at corresponding resolutions to provide matching input fields for the generator. The discriminator that has

been trained during the semi-supervised phase is not further trained. Since no ϕ_{HR} is available as a label during the PUT phase, the generator’s loss simplifies to its continuity and adversarial components,

$$\begin{aligned}\mathcal{L}_{\text{GEN}_{\text{PUT}}} &= \alpha_3 L_{\text{continuity}} + \alpha_4 L_{\text{adversarial}_{\text{PUT}}} \\ L_{\text{continuity}} &= \text{MSE}(\nabla \cdot \phi_{\text{SR}}, 0) \\ L_{\text{adversarial}_{\text{PUT}}} &= -\mathbb{E}[\log(\sigma(D(G(\phi_{\text{LR}})))]) ,\end{aligned}\tag{15}$$

where the standard adversarial loss is employed. Thus, the PUT phase of the generator is exclusively driven by the discriminator’s physics-informed feedback and the continuity constraint.

4.2 Training configurations

Different training configurations are considered. These are primarily distinguishing between the use of multiple ϕ_{LR} of varying resolutions, denoted “multiple,” and the use of a set of single ϕ_{LR} of fixed resolution, denoted “single.” In the “single” training configuration, the ϕ_{LR} resolution is fixed at $n_{\Delta_{\text{LR}}} = 16$ with the corresponding ϕ_{HR} resolution at $n_{\Delta_{\text{HR}}} = 8$. The model is trained exclusively for Re200 and incorporates the additional PUT phase. In the “multiple” training configuration, the model is trained simultaneously for $n_{\Delta_{\text{LR}}} \in 16, 14, 12, 10, 8, 6$ with a fixed upsampling factor of two. Thus, the corresponding ϕ_{HR} counterparts are $n_{\Delta_{\text{HR}}} \in 8, 7, 6, 5, 4, 3$. This configuration is trained for both Re110 and Re200, and the additional PUT phase is optionally considered. Table 3 summarizes the training configurations.

Training configuration	Training dataset	$n_{\Delta_{\text{LR}}}$	$n_{\Delta_{\text{HR}}}$	$N_{\phi_{\text{LR}}}$	$N_{\phi_{\text{HR}}}$	PUT
SG-Re110 (multiple)	Re110	16, 14, 12, 10, 8, 6	8, 7, 6, 5, 4, 3	16 ³	32 ³	Yes
SG-Re200 (single)	Re200	16	8	32 ³	64 ³	Yes
SG-Re200 (multiple)	Re200	16, 14, 12, 10, 8, 6	8, 7, 6, 5, 4, 3	32 ³	64 ³	Yes
SG-Re200 (multiple) - NoPUT	Re200	16, 14, 12, 10, 8, 6	8, 7, 6, 5, 4, 3	32 ³	64 ³	No

Table 3: Summary of the training configurations used for the *similarityGAN* (SG) framework. $n_{\Delta_{\text{LR}}}$ and $n_{\Delta_{\text{HR}}}$ denote the filter sizes applied to generate ϕ_{LR} and ϕ_{HR} from the DNS and employed during the training. $N_{\phi_{\text{LR}}}$ and $N_{\phi_{\text{HR}}}$ specify the sizes of the corresponding training sub-box pairs. The column “PUT” indicates whether the partially unsupervised training phase is applied.

Due to the large amount of training data, loading the entire dataset into GPU memory is impractical. To address this, a patch-to-patch training strategy is applied, in which subboxes are randomly extracted from the full domain for each snapshot [22]. For simplicity, the same training subbox sizes, 64^3 for ϕ_{HR} and 32^3 for ϕ_{LR} , are used across all filter sizes, with an equal number of subboxes per filter regardless of $n_{\Delta_{\text{LR}}}$. These training subbox sizes are found to be ideal for training due to the batch size and box size trade-off associated with finite memory capacity [22].

All training is performed on the CLAIX cluster at RWTH Aachen University using a single node equipped with four NVIDIA H100 GPUs (96 GB each). The total training time of the SG-Re200 (single) setup is approximately 4 hours. When training simultaneously using multiple filter sizes – SG-Re200 (multiple) – the training time increases to approximately 42 hours. The most computationally demanding training configuration is with the PUT phase enabled, for which the training time increases to approximately 65 hours. The computational time required for the LES SR predictions themselves, as well as the associated preprocessing steps, further increases the total time but is not considered in the values mentioned above. For the SG-Re110 (multiple) setup, the training time is reduced by approximately 30% owing to the smaller training subbox pairs.

5 *A priori* investigations of the DMSRM

We first investigate the reconstruction capabilities of the *similarityGAN* framework. Specifically, given ϕ_{LR} at resolution $n_{\Delta_{\text{LR}}}$, *similarityGAN* generates an SR field at resolution $n_{\Delta_{\text{HR}}}$, aiming to generate the corresponding ϕ_{HR} . In this analysis, ϕ_{LR} is obtained using a filter kernel different from those employed to generate the training ϕ_{LR} . This “out-of-sample” kernel distorts the turbulent kinetic energy (TKE) distribution at scales larger than the filter cutoff, mimicking the numerical errors typically encountered in LES. Additional details are given in Appendix A. Since

similarityGAN's reconstruction performance for ϕ_{LR} obtained using “in-sample” filter kernels is known to be strong [20], we do not repeat the “in-sample” analysis here. We conduct subsequent analyses using the Re200 dataset, which allows for large filter widths within the inertial subrange, making the results more relevant to LES of higher Reynolds number flows.

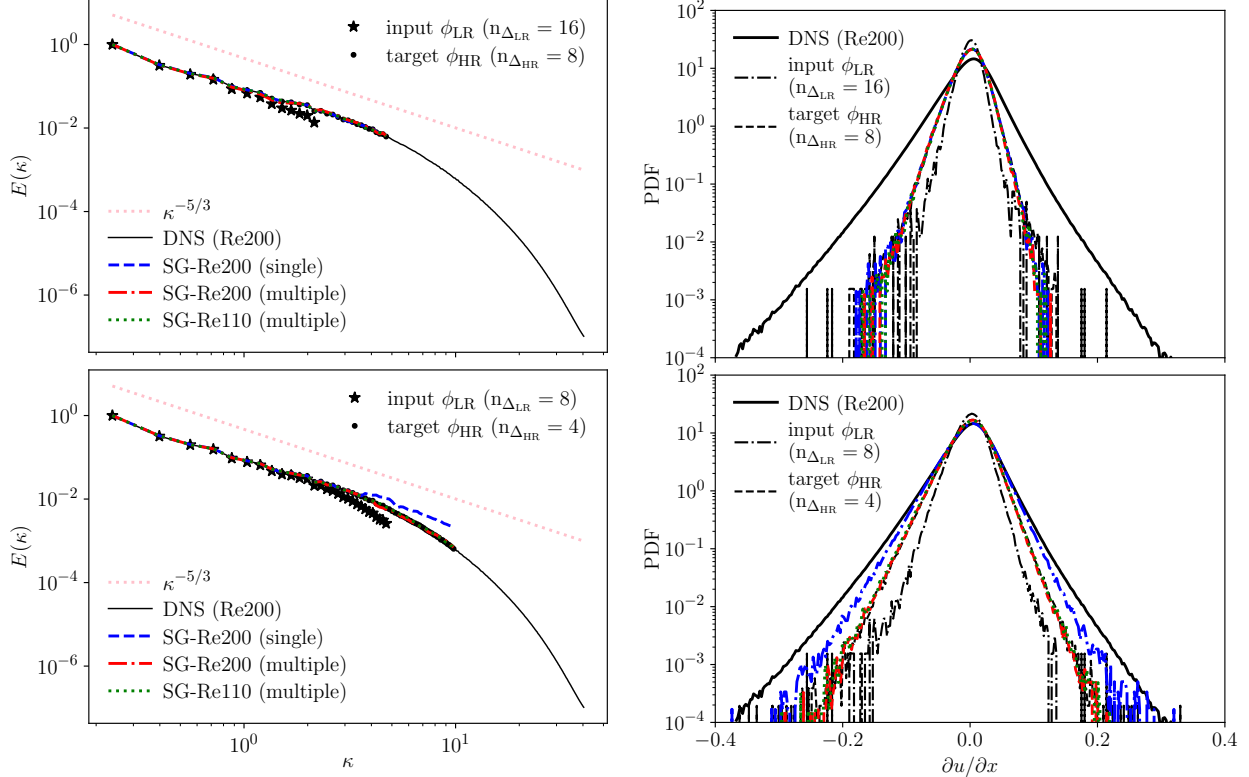


Figure 2: *A priori* normalized TKE spectra (left) and PDFs of $\partial u / \partial x$ (right) for “out-of-sample” input ϕ_{LR} fields from the Re200 dataset. The top row shows results for $n_{\Delta_{LR}} = 16$, and the bottom row for $n_{\Delta_{LR}} = 8$. “SG-Re200 (single)” and “SG-Re200 (multiple)” refer to the *similarityGAN* framework trained on the Re200 dataset using either a single fixed ϕ_{LR} resolution or multiple varying ϕ_{LR} resolutions, respectively. “SG-Re110 (multiple)” refers to the same framework trained on the Re110 dataset with multiple varying ϕ_{LR} resolutions (see table 3). For clarity, red and green lines overlap with the target ϕ_{HR} line.

Figure 2 shows TKE spectra (left) and probability density functions (PDFs) (right) of one component of the velocity gradient, $\partial u / \partial x$, of the SR fields obtained using the three training configurations with the PUT phase, as described in table 3. Results are given for two input ϕ_{LR} resolutions: $n_{\Delta_{LR}} = 16$ in the top row and $n_{\Delta_{LR}} = 8$ in the bottom row. The SG-Re200 (multiple) training configuration demonstrates strong reconstruction performance at both resolutions. The TKE spectra closely match the target ϕ_{HR} , and PDFs of $\partial u / \partial x$ reflect accurate fine-scale statistics, even under “out-of-sample” filter kernel conditions. In contrast, the SG-Re200 (single) training configuration performs well only for $n_{\Delta_{LR}} = 16$, but fails to reproduce small-scale velocity fluctuations and overpredicts the TKE spectra for the unseen input resolution $n_{\Delta_{LR}} = 8$. These results indicate that training with ϕ_{LR} of varying resolutions preserves the reconstruction accuracy across different input resolutions. This is important for *a posteriori* deployment of the *similarityGAN* framework, even when training and testing are performed using the same dataset, since the LES filter kernel and size are not known [36].

Another important aspect for practical *a posteriori* deployment is generalizability to higher Reynolds numbers. This is demonstrated in figure 2, which shows TKE spectra and velocity-gradient PDFs of SR fields obtained by applying the SG-Re100 (multiple) model to upsample Re200 ϕ_{LR} fields at resolutions of $n_{\Delta_{LR}} = 16$ and $n_{\Delta_{LR}} = 8$. Despite being trained for lower Reynolds number flow, the SG-Re100 (multiple) training configuration exhibits good performance when applied to the Re200 dataset, closely reconstructing the TKE spectra and velocity-gradient PDF at the two $n_{\Delta_{LR}}$ ratios. We therefore select the multiple-training configuration for the DMSRM (Eq. (12)) for all subsequent analyses.

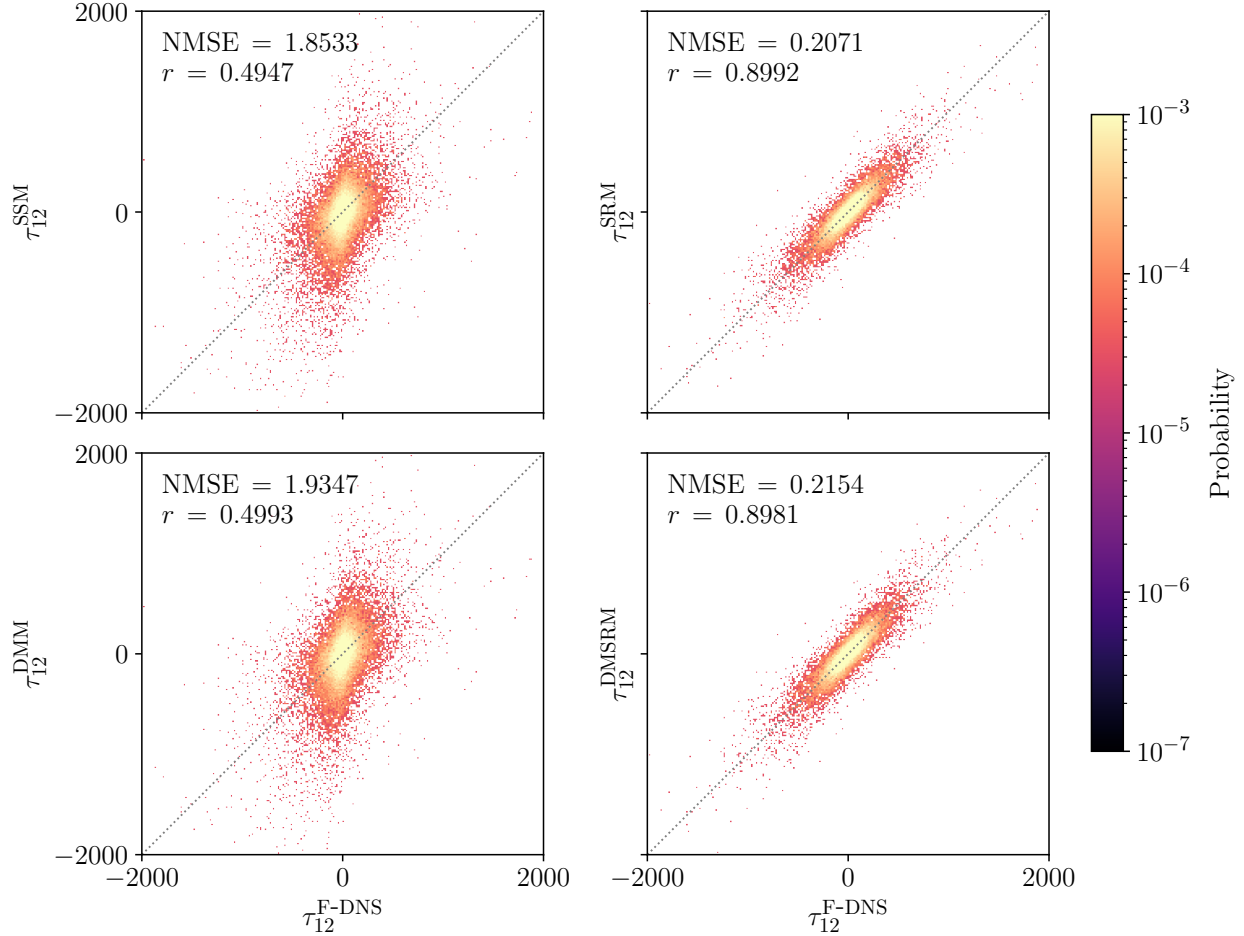


Figure 3: jPDFs of the F-DNS reference of the SFS stress tensor component $\tau_{12}^{\text{F-DNS}}$ and the SSM component τ_{12}^{SSM} (upper left), the SRM component τ_{12}^{SRM} (upper right), the DMM component τ_{12}^{DMM} (lower left), and the DMSRM component τ_{12}^{DMSRM} (lower right), evaluated for a test snapshot of the Re200 dataset at $n_{\Delta_{\text{LR}}} = 16$. SRM and DMSRM τ_{12} components are evaluated using the SR field obtained using the SG-Re200 (multiple) training configuration. ‘‘NMSE’’ indicates the normalized MSE.

The effectiveness of DMSRM is further examined through *a priori* correlations of the SFS stress tensor component τ_{12} . Figure 3 shows joint PDFs (jPDFs) of the FDNS-evaluated SFS stress component τ_{12} and the analogous component evaluated using the DMM (left) and the DMSRM (right). The top row of figure 3 includes only the scale-similarity and super-resolution contributions; the bottom row includes the dynamic Smagorinsky contribution. The Pearson correlation coefficient, r , for the SRM is approximately twice that of the SSM, indicating a significantly improved agreement with the DNS. The superior performance of the SRM demonstrates that estimating the scale-similarity term from the SR velocity field provides more accurate SFS stress predictions than the standard SSM.

It is worth noting that the distributions obtained with the DMM and DMSRM closely match the corresponding scale-similarity and super-resolution contributions, indicating that the scale-similarity term is much larger than the DSM contribution. Interestingly, the dynamic Smagorinsky contribution to the DMM marginally increases the correlation coefficient, while in the DMSRM, it marginally decreases it. While not shown here, similar trends are observed for the finer input resolution with $n_{\Delta_{\text{LR}}} = 8$.

Further insight is provided in figure 4 (left), which shows the PDFs of τ_{12} obtained from the DMM, DMSRM, and their individual components (see Eqs. (5) and (12)) compared against the F-DNS reference. The PDF of the SRM nearly overlaps with the F-DNS, both in peak location and tail behavior, suggesting that the SRM accurately reconstructs the SFS stress both pointwise (figure 3, top-right) and statistically. In contrast, the PDF of the SSM overpredicts high-magnitude stresses, characterized by a broader distribution compared to the F-DNS, which is consistent with prior observations (figure 3, top-left). As is also evident from the previous analysis, the scale-similarity components clearly

dominate the PDF of τ_{12} in the dynamic mixed formulations, as both the “DSM \rightarrow DMM” and “DSM \rightarrow DMSRM” PDFs are significantly narrower.

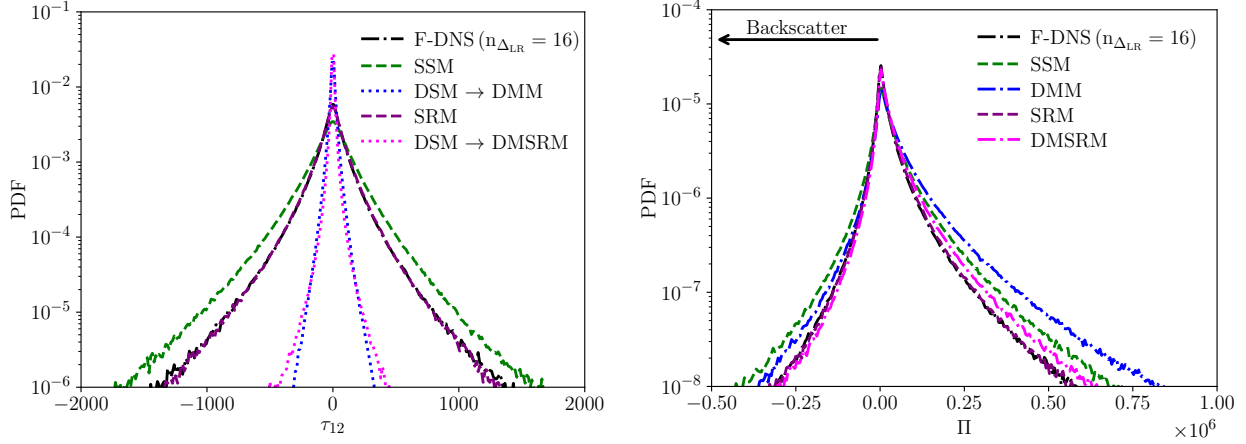


Figure 4: PDFs of τ_{12} (left) and Π (right) obtained from the DMM, DMSRM, and their individual components compared against the F-DNS reference (see Section 2), using the Re200 dataset.

The SFS energy dissipation, $\Pi = -\tau_{ij}\bar{S}_{ij}$, quantifies the energy transfer between resolved and subfilter scales, with positive values indicating dissipation and negative values indicating backscatter. Figure 4 (right) also shows the PDFs of Π obtained with the DMM, DMSRM, and their individual components compared against the F-DNS. As expected, the SSM exhibits excessive backscatter, a behavior that can lead to numerical instabilities in *a posteriori* simulations. The SSM also overpredicts SFS energy dissipation. Combining the SSM with the DSM (i.e., the DMM) mitigates the excessive backscatter thanks to the DSM’s dissipative nature. However, this correction comes at the cost of increased dissipation relative to the F-DNS. Conversely, the SRM alone provides a much closer match to the F-DNS in terms of dissipation and backscatter. When combined with the DSM, a slight overprediction of the dissipation is apparent, while its impact on backscatter remains minimal. Interestingly, while the DMM yields an improved prediction of SFS energy dissipation compared to the SSM, it still overpredicts the stress tensor components. In contrast, the SRM alone already achieves an accurate reconstruction of the SFS stress components and the SFS energy dissipation. This *a priori* analysis suggests that the inclusion of the DSM may introduce excessive dissipation, potentially degrading the DMSRM’s overall fidelity, though it may still be required for numerical stability in *a posteriori* settings, which we investigate in the next section.

6 *A posteriori* investigations of the DMSRM

6.1 Physical accuracy of the DMSRM

We next evaluate the predictive fidelity of the DMSRM using *a posteriori* LES. We simulate the Re200 configuration (see Section 3) using an identical forcing using two LES grids of resolution 32^3 , corresponding to $n_{\Delta_{LR}} = 16$ ($\Delta_{LR}/\eta \approx 27$), and 64^3 , corresponding to $n_{\Delta_{LR}} = 8$ ($\Delta_{LR}/\eta \approx 13$). Two DMSRM configurations are considered. “DMSRM 200” employs the *similarityGAN* model trained on the SG-Re200 (multiple) training, while “DMSRM 110” uses the SG-Re110 (multiple) model. The latter is used to evaluate the DMSRM’s ability to generalize to a higher Reynolds number flow. Results are compared against the reference F-DNS, obtained with a spectral filter kernel operator with consistent Δ_{LR} .

Figure 5 shows the TKE spectra (left) and PDFs of $\partial u / \partial x$ (right) for the coarse (top row) and fine (bottom row) LES resolutions. At the coarse resolution ($n_{\Delta_{LR}} = 16$), both DMSRMs are in close agreement with the F-DNS and outperform the DMM. The differences between the two DMSRM configurations are small. DMSRM 200 achieves the most accurate performance, captures the inertial subrange scaling and maintains TKE levels close to those of the F-DNS throughout all turbulent scales. Good agreement is also observed for the velocity gradient PDFs, which show well-predicted heavy tails, indicating successful modeling of small-scale intermittency. DMSRM 110 shows similar trends, albeit with a mild underprediction of TKE near the grid cut-off (shown in the insets) and a corresponding narrowing of the velocity gradient PDF. This suggests a modest loss of accuracy when extrapolating to higher Reynolds numbers, which could be anticipated of any offline-trained neural network model. The DMM exhibits a clear deviation

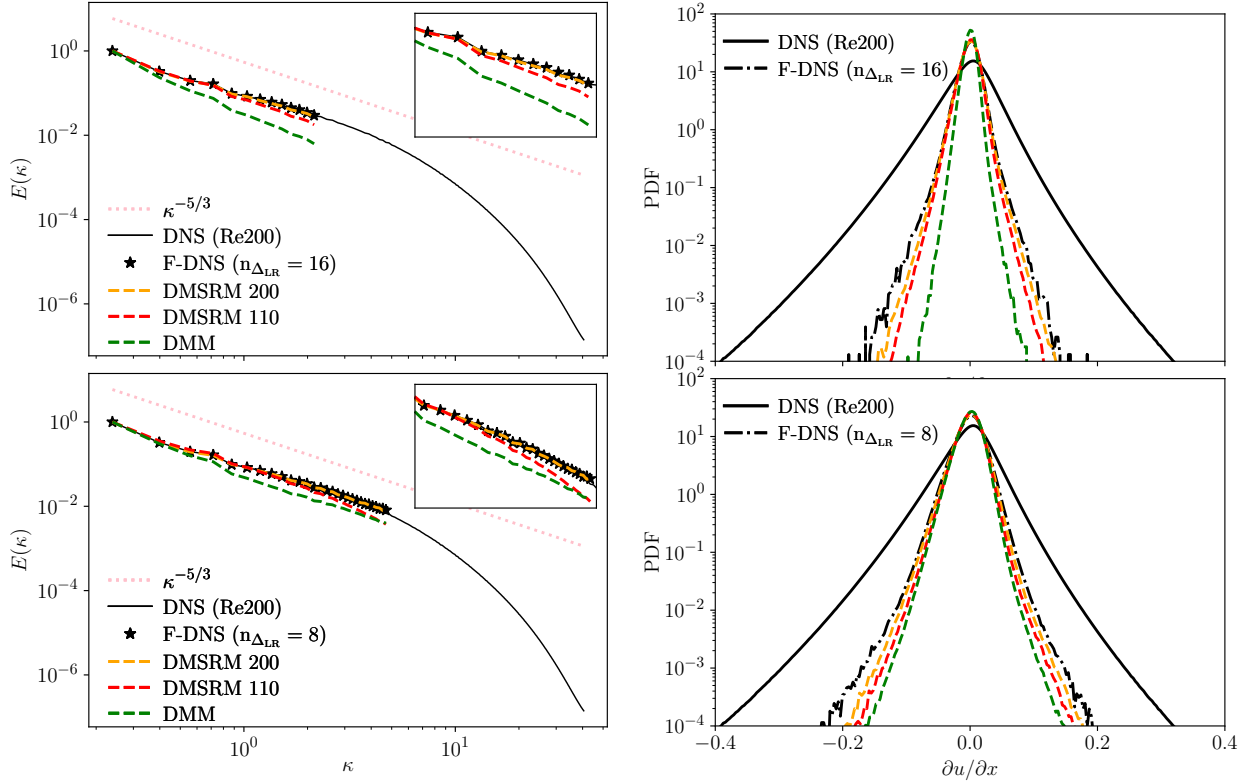


Figure 5: *A posteriori* normalized TKE spectra (left) and PDFs of $\partial u / \partial x$ (right) of LES coarsened by $n_{\Delta_{LR}} = 16$ (top row) and $n_{\Delta_{LR}} = 8$ (bottom row) from the Re200 DNS. F-DNS fields are obtained with a spectral filter kernel operator with consistent Δ_{LR} . The “DMSRM 200” uses the SG-Re200 (multiple) model, while “DMSRM 110” uses the SG-Re110 (multiple).

from the TKE spectra, particularly by underpredicting intermediate- and high-wavenumber energy, which reflects its overly dissipative behavior. This is also seen in its narrower velocity gradient PDF, indicating suppressed turbulence intermittency. At the finer resolution ($n_{\Delta_{LR}} = 8$), the differences between all dynamic mixed models decrease, while their overall trends remain similar.

To provide insight into the reasons for the above observations, figure 6 shows PDFs of Π for both DMSRMs and the DMM against the F-DNS reference at the coarse (left) and fine (right) resolutions. At the coarse resolution, both DMSRMs exhibit good agreement with the F-DNS, with DMSRM 200 achieving the closest agreement with the F-DNS across both positive and negative values of Π , while DMSRM 110 is slightly more dissipative. In contrast, the DMM substantially overpredicts the SFS energy dissipation and underestimates backscatter. This imbalance is rooted in a well-known limitation of SSMs, which tend to generate excessive backscatter and can become unstable due to uncontrolled energy transfer from the subfilter to the resolved scales. To mitigate this effect, DMMs introduce a dissipative DSM term, but this correction leads to overly damped turbulence dynamics and suppression of backscatter. This observation is consistent with the *a priori* analyses presented in Section 5.

These observations are quantified through the relative impact of backscatter to the total SFS energy dissipation, which is defined as,

$$B_{\Pi} = -\frac{\langle \min(\Pi^{\text{model}}, 0) \rangle_t}{\langle \Pi^{\text{model}} \rangle_t} \text{ with } \Pi^{\text{model}} = -\tau_{ij}^{\text{model}} \bar{S}_{ij}, \quad (16)$$

where $\langle \cdot \rangle_t$ denotes averaging over the spatial domain and an ensemble of LES snapshots, and the superscript denotes the selected closure model for τ_{ij} . At the coarse resolution, backscatter computed from F-DNS accounts for approximately 20% of Π . The SRM contributions obtained with SG-Re200 and SG-Re110 yield backscatter levels of approximately 19% and 18%, respectively, close to the F-DNS. When these SRMs are combined with the DSM contribution, the DMSRM net backscatter remains similar, with values of approximately 18% (SG-Re200) and 16% (SG-Re110). In contrast, the SSM alone predicts a larger fraction of 27%, which is reduced substantially to approximately 9% with the DMM formulation. While this reduction enhances numerical stability, it also reflects the overly

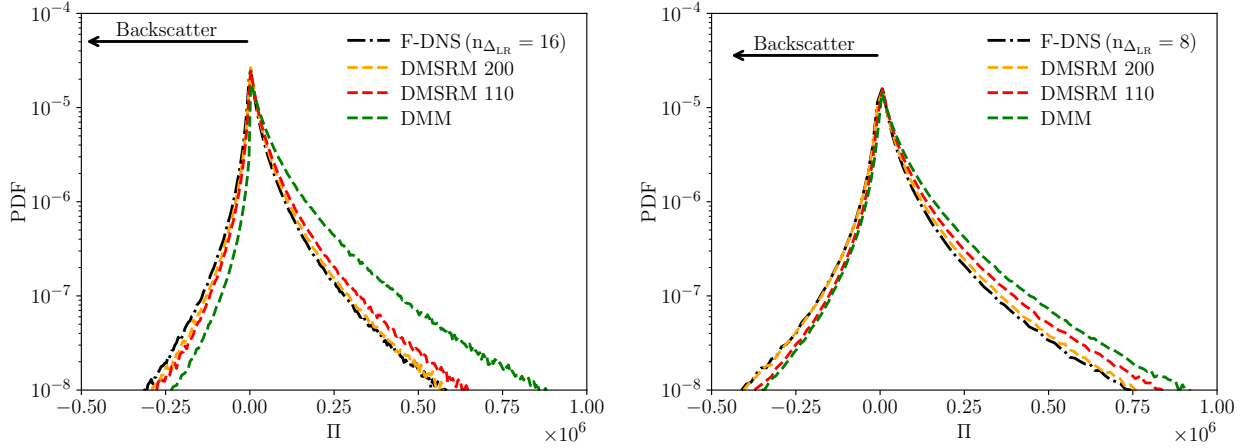


Figure 6: *A posteriori* PDFs of II for both DMSRM setups and the DMM against the F-DNS reference at coarser (left) and finer (right) resolutions.

dissipative nature of the DMM. At the fine resolution, the overprediction of SFS energy dissipation for the DMM is decreased, and backscatter is increased (approximately to 11%) and is more similar to the F-DNS (approximately to 13%). Both DMSRMs maintain their accurate backscatter prediction, with backscatter values very close to the F-DNS value.

This trend is also reflected in the averaged C_d^2 , which is evaluated from the DSM contributions to the DMSRM and DMM. At the coarse resolution, values of 0.07 and 0.09 are obtained for DMSRM 200 and DMSRM 100, respectively, compared to 0.13 for the DMM. A similar pattern with decreased values is observed at the fine resolution. Additionally, the DMM exhibits greater C_d^2 scatter than the DMSRMs, which is consistent with its less accurate representation of local SFS stresses [37].

These results highlight that an accurate scale-similarity contribution is essential for achieving close agreement with the F-DNS. Backscatter is reproduced through the scale-similarity term, which in turn controls the DSM contribution and ensures consistent mean energy transfer across scales. In this regard, the DMSRM outperforms the DMM. Its advantage lies in the data-driven SR-GAN framework, which is trained on high-fidelity data and optimized with an adversarial loss; therefore, super-resolved velocity fields that are physically plausible are reconstructed. The SFS stress tensor at the grid-filter scale is then obtained directly from such SR fields using a filter kernel and size consistent with training, yielding SFS stress that are of correct magnitudes and accurately reproduce dissipation. This reduces reliance on additional dissipation provided by the DSM term and maintains physically consistent backscatter. As a result, the SR-based approach produces a physically and numerically consistent reconstruction than both the LES and SR test-filtered fields, making it a robust alternative to the traditional SSM in the DMM formulation.

6.2 Stability of the DMSRM

The previous analyses of the DMSRM show that the DSM contribution is small, raising the question of its necessity within the model formulation. In the absence of the DSM contribution, the DMSRM reduces to the SRM (Eq. (12)). For the following tests, the SG-Re200 (multiple) training is employed, and the coarse resolution with $n_{\Delta_{LR}} = 16$ is considered. This variant is hereafter referred to as “SRM 200”.

The performance of SRM 200 compared with the reference F-DNS is shown in figure 7 using TKE spectra (left) and the PDF of $\partial u / \partial x$ (right). The results from DMSRM 200 and the DMM are also included. SRM 200 remains numerically stable even without the DSM term and still outperforms the DMM. However, the TKE spectra show a slight accumulation of energy near the cut-off wavenumber, and the PDF of $\partial u / \partial x$ is narrowed compared to the results obtained using DMSRM 200. Although the DSM contribution in DMSRM 200 is small, these findings suggest that it plays an important role in achieving accurate physical predictions, particularly for wavenumbers near the cut-off filter.

The stability and accuracy of SRM 200 suggest that the DMSRM’s robust performance primarily stems from the ability of the *similarityGAN* framework to reconstruct physically accurate u^* fields, even for unseen ϕ_{LR} . To evaluate this aspect, the PUT phase is omitted from the *similarityGAN* training, and the weights and biases obtained are used in both SRM and DMSRM. These models are denoted “SRM 200 (NoPUT)” and “DMSRM 200 (NoPUT).” As shown

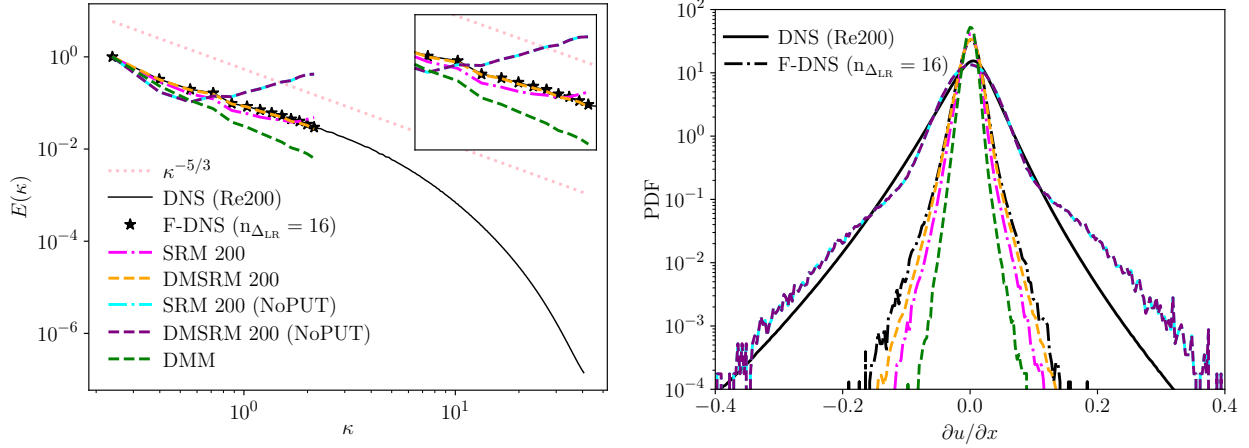


Figure 7: *A posteriori* normalized TKE spectra (left) and PDFs of $\partial u / \partial x$ (right) for Re200 at LES mesh ratio $n_{\Delta_{LR}} = 16$. “DMSRM 200” and “SRM 200” use the SG-Re200 (multiple) model, while “DMSRM 200 (NoPUT)” and “SRM 200 (NoPUT)” use the SG-Re200 (multiple) - NoPUT model (see table 3).

in figure 7, both models yield similar predictions to those of implicitly modeled (“no-model”) LES. Interestingly, the DSM contribution to DMSRM 200 (NoPUT) does not improve the overall performance, indicating that it does not provide enough dissipation under these conditions.

To further evaluate the reconstruction capabilities of the *similarityGAN* and the physical fidelity of SR fields generated by the *similarityGAN* from unseen inputs, the same coarse-resolution DMM velocity fields (denoted “input DMM ($n_{\Delta_{LR}} = 16$ ”) are provided as input to either the SG-Re200 or SR-Re200 - NoPUT models. As shown in figure 8 (left), the corresponding u^* fields generated by the PUT-trained model closely match the F-DNS spectra at the corresponding $n_{\Delta_{HR}}$, whereas omitting the PUT phase leads to a pronounced overprediction of the TKE at the SFS scales. The resulting u^* fields are then unphysical and destabilize the simulations. This is highlighted in figure 8 (right), where only the DMSRM 200 closely matches the F-DNS across both positive and negative Π values. Conversely, in the absence of the PUT phase, the Π distribution obtained from DMSRM 200 - NoPUT is unphysical, exhibiting excessive backscatter and insufficient SFS energy dissipation. This imbalance cannot be mitigated by simply adding a dissipative-only DSM term, because the *similarityGAN* model itself produces unphysical u^* fields. In such cases, the on-the-fly stabilization mechanism provided by the DSM term is insufficient to recover a physically meaningful prediction. This suggests that adequate generalization capabilities to unseen input fields are essential for stable and accurate *a posteriori* performance. Nevertheless, even with nearly perfect SR reconstruction, the DSM contribution remains important to obtain correct net energy dissipation.

7 Computational efficiency of the DMSRM

In addition to predictive accuracy and stability, computational efficiency is important for the practical deployment of SFS models. Table 4 summarizes the computational inference costs and memory requirements of the *similarityGAN*’s generator when employed to super-resolve ϕ_{LR} of different resolutions, denoted $N_{\phi_{LR}}$, corresponding to the LES grid resolutions of Section 6. Two upsampling factors are considered: a factor of two, which is used in the DMSRM, and a larger factor required to reconstruct fields at DNS resolution from the given input resolutions. The larger upsampling factor analysis is included to enable comparison with previous studies, as available works in the literature report analyses upsampled to DNS resolution. For upsampling to DNS resolution, additional upsampling layers are added in sequence in the *similarityGAN* framework (see figure 1).

The peak memory requirements and inference times increase significantly with both upsampling factor and $N_{\phi_{LR}}$. For an upsampling factor of two, memory requirements are modest and GPU inference provides an order-of-magnitude speed-up compared to the CPUs for both input resolutions, highlighting the suitability of GPUs for accelerating SR-LES workflows with large DL models.

The *a posteriori* computational overhead of the DMSRM relative to the DMM is also reported in table 4 for an upsampling factor of two. Both the runtime and memory requirements are shown. Measurements are averaged over the same 50 timesteps, and the same numerical schemes and pressure solver are used. Initialization routines are excluded from the runtime computations. Due to current challenges in parallelizing SR-based LES, all simulations are conducted

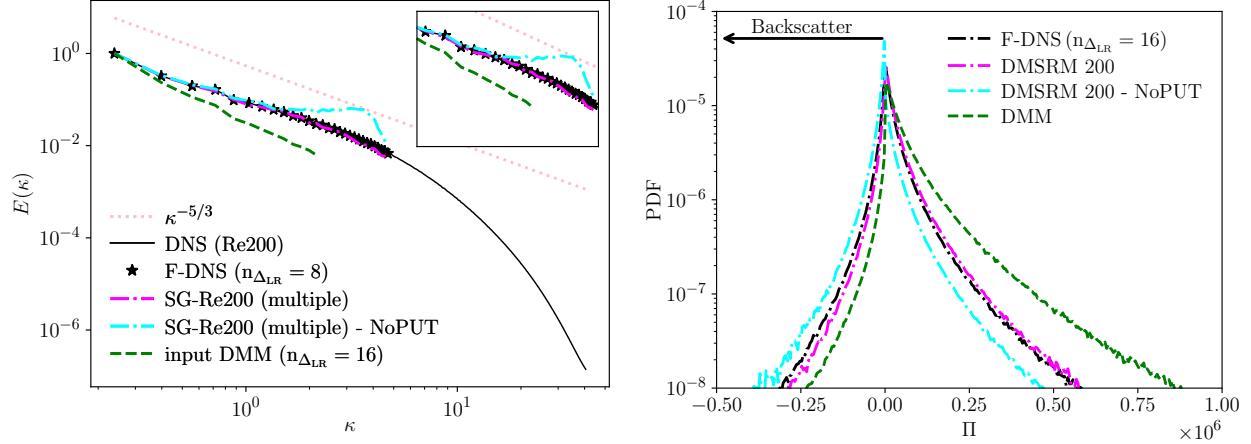


Figure 8: Comparison of the normalized TKE spectra (left) and PDFs of Π computed using the super-resolved fields obtained using either “SG-Re200 (multiple)” or “SG-Re200 (multiple) - NoPUT” models. The same coarse resolution DMM velocity fields (denoted “input DMM”) are provided as input velocity fields. The F-DNS and DMM results are reported for reference. “DMSRM 200 - NoPUT” refers to as the DMSRM using the “SG-Re200 (multiple) - NoPUT” model.

$N_{\phi_{LR}}$	Upsampling factor	Inference memory (peak)	Inference wall time		DMSRM overhead (%) vs DMM)		
			CPUs	GPU	Memory (peak)	CPUs runtime	GPU runtime
32^3	2	≈ 0.75 GB	0.47 s	0.053 s	224%	102%	13%
32^3	16	≈ 112 GB	52.27 s	N/A	—	—	—
64^3	2	≈ 3.31 GB	1.83 s	0.197 s	321%	123%	19%
64^3	8	≈ 110 GB	50.31 s	N/A	—	—	—

Table 4: Computational inference requirements of *similarityGAN*’s generator for different input field sizes $N_{\phi_{LR}}$ and upsampling factors. Reported metrics include peak memory usage and wall time on CPU (96-core Intel Sapphire Rapids) and GPU (NVIDIA H100 96 GB). “N/A” indicates a memory limitation that prevents execution. All values refer to a single-sample inference. For upsampling factor 2, the *a posteriori* computational overhead of the DMSRM relative to the traditional DMM is also reported, both in terms of memory footprint and runtime cost.

in serial to avoid potential biases arising from differences in GPU and CPU parallelization strategies [38]. For both the DMM and the DMSRM, one CPU-only execution is performed, while for the DMSRM an additional setup combining one CPU core and one GPU is also considered. Consequently, none of the LESs employ domain decomposition. The DMSRM exhibits considerably larger memory requirements than the DMM (224% and 321% overhead for $N_{\phi_{LR}} = 32^3$ and $N_{\phi_{LR}} = 64^3$, respectively), primarily due to the storage of intermediate fields of increased resolution needed by the inference operation. The runtime overhead of the DMSRM is substantial when using CPU-only execution (approximately 100–120%), whereas employing one CPU core and one GPU dramatically reduces the overhead to approximately 13% and 19% for the coarse and fine LES grid resolutions, respectively. The differences to the DMM arise mainly from CPU–GPU communication, inference, and filtering/downsampling operations at multiple scales (see Eq. (12)). On GPUs, however, the additional cost is modest, and the overall cost of the DMSRM remains limited. The low computational cost of the DMSRM, particularly when leveraging GPUs, makes it suitable for practical SR-LES applications, especially considering its improved physical accuracy.

It must be noted that the memory demand peaks at approximately 110 GB, surpassing the capacity of high-end GPUs such as the NVIDIA H100 (96 GB) for upsampling factors up-to-DNS resolutions. Consequently, GPU inference is challenging, and CPU inference is slow, exceeding 50 s. This substantial cost escalation is driven by the non-linear scaling of the convolutional operations, activation maps, and intermediate tensors, as well as overhead from the TensorFlow library. These findings emphasize the trade-off between resolution enhancement and computational feasibility of SR-based models and demonstrate that upsampling to DNS resolution is impractical. Decreased upsampling factors are essential to ensure practicality, especially for large-scale SR-LES applications.

8 Conclusion

A novel hybrid dynamic super-resolution-based mixed model is presented, which combines the robustness and computational efficiency of dynamic mixed models with the physically consistent velocity reconstructions of SR-GAN frameworks, here obtained using *similarityGAN*. In the DMSRM, the velocity fields are super-resolved to finer-than-LES resolutions, and both the scale-similarity term and the dynamic Smagorinsky term are evaluated using the resulting inter-scale range. The physical fidelity of the resulting SFS stress closure is improved compared to conventional DMMs without the prohibitive need to upsample to DNS-scale resolutions as in previous SR-based closure approaches.

A priori analyses on forced homogeneous isotropic turbulence demonstrate that the *similarityGAN* framework accurately reconstructs super-resolved velocity fields, even for “out-of-sample” filter conditions. Training with multiple input resolutions is essential for maintaining accuracy across varying input filter sizes, and the framework is also shown to generalize well to higher Reynolds number flows of the same configuration. The scale-similarity term evaluated at the SR-grid level accurately reproduces pointwise and statistical features of the DNS SFS stress tensor, whereas traditional scale-similarity models tend to overpredict the magnitude of the stresses and backscatter. The DSM contribution is minor in *a priori* tests, suggesting that the super-resolution component alone could serve as an accurate closure model.

A posteriori tests confirm that the DMSRM improves the predictive capability and physical fidelity relative to the DMM for different LES resolutions. For very coarse LES, the DMSRM accurately captures the TKE spectra, velocity gradient PDFs, and small-scale intermittency. Analyses of SFS energy dissipation show that the DMSRM predicts correct levels of backscatter, unlike the DMM, which tends to underestimate backscatter and overpredict SFS dissipation. No strong sensitivity to the Reynolds number of the training dataset is observed for the DMSRM, suggesting adequate generalization capabilities to similar flow configurations. For finer LES, differences between models are less pronounced, yet the DMSRM consistently improves upon the DMM by preserving small-scale structures and avoiding excessive dissipation.

These investigations further demonstrate that an accurate scale-similarity contribution is essential for achieving close agreement with F-DNS, while the DSM term plays a secondary role by ensuring energy balance at the cut-off scale and exerts a stabilizing effect. The superior performance of the DMSRM primarily stems from the physically consistent super-resolved velocity fields generated by *similarityGAN* and its strong generalization to unseen inputs. This capability is enabled by the partially unsupervised training phase, in which the discriminator functions as a physics-informed component and the generator is guided through adversarial feedback to produce physically plausible SR fields, even for unseen input fields. The SFS stress tensor estimation at the grid-filter scale is then obtained directly from such SR fields using an explicit filter kernel and size consistent with training, yielding stresses that are of correct magnitudes, and dissipation is reproduced accurately. The computational costs of the DMSRM are also manageable. The moderate upsampling factors employed by the DMSRM keep inference efficient.

Overall, the DMSRM achieves improved physical fidelity at a reasonable computational overhead, making it a robust and practical alternative to traditional DMMs for LES. Although the present study focuses on homogeneous isotropic turbulence, the DMSRM could be extended to inhomogeneous flows. For free-shear flows, reasonable performance may be expected since only the smallest scales, typically near-isotropic, are super-resolved. Future work will focus on extending the DMSRM formulation to variable-density flows and applying it to wall-bounded turbulent flows, where additional physical constraints may be required to ensure physically consistent SR velocity and scalar fields. Furthermore, overcoming current challenges in the generalization capabilities of the SR-GAN framework across different flow configurations will be essential for practical deployment.

Acknowledgments

The research leading to these results has received funding from the German Federal Ministry of Education and Research (BMBF) and the state of North Rhine-Westphalia for supporting this work as part of the NHR funding and the European Union under the European Research Council Advanced Grant HYDROGENATE, Grant Agreement No. 101054894. The authors thank S. Sakhare for his exceptional support and contribution to this research project. Computations were performed with computing resources granted by RWTH Aachen University under project *rwh1387*.

A Definition of filter kernel and downsampling operators

The definitions of the spatial box, Gaussian, spectral, and modified-Gaussian (MG) filter kernels are

$$\mathcal{G}_{\text{box}}(\mathbf{r}) = \begin{cases} \frac{1}{\Delta} & \text{if } |\mathbf{r}| \leq \frac{\Delta}{2} \\ 0 & \text{otherwise} \end{cases} \quad (17)$$

$$\mathcal{G}_{\text{Gaussian}}(\mathbf{r}) = \left(\frac{6}{\pi \Delta^2} \right)^{\frac{1}{2}} \exp \left(-\frac{6\mathbf{r}^2}{\Delta^2} \right), \quad (18)$$

$$\mathcal{G}_{\text{spectral}}(\mathbf{r}) = \frac{\sin(\pi \mathbf{r}/\Delta)}{\pi \mathbf{r}} \quad (19)$$

$$\mathcal{G}_{\text{MG}}(\mathbf{r}) = \left(\frac{\beta}{\pi \Delta^2} \right)^{1/2} \exp \left(-\frac{\beta \mathbf{r}^2}{\Delta^2} \right). \quad (20)$$

Here, the filter width Δ is set to either Δ_{LR} or Δ_{HR} , depending on whether the ϕ_{LR} or ϕ_{HR} fields are considered, as detailed in Section 3. The filter operator in Eq. (20) is applied to generate the “out-of-sample” ϕ_{LR} fields used for the *a priori* tests in Section 5. In particular, for the MG kernel, the parameter $\beta = 3$ is chosen to introduce TKE distortion near the cut-off filter scale. This ensures that the test fields differ systematically from those generated with the box, Gaussian, and spectral filter kernels used to generate the training ϕ_{LR} fields (see Section 3). The downsampling operator, applied independently of the filter kernel, maps the velocity field from Ω^* to $\bar{\Omega}$ by simply subsampling. For a decimation factor of two, it reads

$$\check{\mathbf{u}}(I, J, K) = \mathbf{u}(2I, 2J, 2K), \quad I = 0, \dots, \bar{N}_x - 1, \quad J = 0, \dots, \bar{N}_y - 1, \quad K = 0, \dots, \bar{N}_z - 1, \quad (21)$$

where $\check{\mathbf{u}}$ is the downsampled velocity field and $\bar{N}_x, \bar{N}_y, \bar{N}_z$ are the number of coarse-grid points in each direction (see table 1).

B Calculation of the dynamic model coefficient for the DMM

The DMM used for comparison is defined as

$$\tau_{ij}^{\text{DMM}} = -2C_d^2 \bar{\Delta}^2 |\bar{S}| \bar{S}_{ij} + \tau_{ij}^{\text{SSM}}, \quad (22)$$

where \bar{S}_{ij} and $|\bar{S}|$ defined in Eq. (4), and τ_{ij}^{SSM} in Eq. (6). The dynamic model coefficient C_d^2 is obtained by substituting Eq. (22) into the Germano identity, analogous to Eq. (9), giving

$$\begin{aligned} H_{ij} + C_d^2 M_{ij} &= L_{ij} \text{ with } L_{ij} = \widehat{\bar{u}_i \bar{u}_j} - \widehat{\bar{u}_i} \widehat{\bar{u}_j} \\ M_{ij} &= -2\bar{\Delta}^2 (4|\bar{S}| \bar{S}_{ij} - |\bar{S}| \widehat{\bar{S}}_{ij}). \end{aligned} \quad (23)$$

The tensor H_{ij} is defined as

$$H_{ij} = \widetilde{\bar{u}_i \bar{u}_j} - \widetilde{\bar{u}_i} \widetilde{\bar{u}_j} - (\widehat{\bar{u}_i \bar{u}_j} - \widehat{\bar{u}_i} \widehat{\bar{u}_j}), \quad (24)$$

with notations and operators defined in table 1.

The dynamic model coefficient C_d^2 is then computed using a least-squares error approach, such that

$$C_d^2 = \frac{\langle M_{ij} (L_{ij} - H_{ij}) \rangle}{2 \langle M_{ij} M_{ij} \rangle}, \quad (25)$$

where $\langle \cdot \rangle$ denotes averaging over homogeneous directions to ensure numerical stability. Definitions in Eq. 24 and Eq. (25) might differ from prior works, e.g., in [9–12], due to differences in the SSM definition, the number of dynamic parameters involved, and operators employed among the different filter scales.

References

[1] U. Piomelli and J. R. Chasnov, “Large-eddy simulations: theory and applications,” in *Turbulence and Transition Modelling: Lecture Notes from the ERCOFTAC/IUTAM Summerschool held in Stockholm, 12–20 June, 1995*. Springer, 1996, pp. 269–336.

[2] P. A. Durbin, “Some recent developments in turbulence closure modeling,” *Annual Review of Fluid Mechanics*, vol. 50, pp. 77–103, 2018.

[3] P. Sagaut and C. Meneveau, *Large Eddy Simulation for Incompressible Flows: An Introduction*, ser. Scientific Computation. Springer, 2006, no. 7.

[4] H. Pitsch, “Large-eddy simulation of turbulent combustion,” *Annual Review of Fluid Mechanics*, vol. 38, no. Volume 38, 2006, pp. 453–482, 2006. [Online]. Available: <https://www.annualreviews.org/content/journals/10.1146/annurev.fluid.38.050304.092133>

[5] M. Germano, U. Piomelli, P. Moin, and W. H. Cabot, “A dynamic subgrid-scale eddy viscosity model,” *Physics of Fluids A: Fluid Dynamics*, vol. 3, no. 7, pp. 1760–1765, 07 1991.

[6] C. Meneveau and J. Katz, “Scale-invariance and turbulence models for large-eddy simulation,” *Annual Review of Fluid Mechanics*, vol. 32, no. 1, pp. 1–32, 2000.

[7] J. Bardina, *Improved turbulence models based on large eddy simulation of homogeneous, incompressible, turbulent flows*. Stanford University, 1983.

[8] S. Liu, C. Meneveau, and J. Katz, “On the properties of similarity subgrid-scale models as deduced from measurements in a turbulent jet,” *Journal of Fluid Mechanics*, vol. 275, pp. 83–119, 1994.

[9] Y. Zang, R. L. Street, and J. R. Koseff, “A dynamic mixed subgrid-scale model and its application to turbulent recirculating flows,” *Physics of Fluids A: Fluid Dynamics*, vol. 5, no. 12, pp. 3186–3196, 1993.

[10] R. Anderson and C. Meneveau, “Effects of the similarity model in finite-difference LES of isotropic turbulence using a Lagrangian dynamic mixed model,” *Flow, Turbulence and Combustion*, vol. 62, pp. 201–225, 1999.

[11] B. Vreman, B. Geurts, and H. Kuerten, “On the formulation of the dynamic mixed subgrid-scale model,” *Physics of Fluids*, vol. 6, no. 12, pp. 4057–4059, 1994.

[12] M. V. Salvetti and S. Banerjee, “A priori tests of a new dynamic subgrid-scale model for finite-difference large-eddy simulations,” *Physics of Fluids*, vol. 7, no. 11, pp. 2831–2847, 1995.

[13] A. Scotti and C. Meneveau, “Fractal model for coarse-grained nonlinear partial differential equations,” *Physical Review Letters*, vol. 78, pp. 867–870, Feb 1997. [Online]. Available: <https://link.aps.org/doi/10.1103/PhysRevLett.78.867>

[14] J. M. McDonough, S. Mukerji, and S. H. Chung, “A data-fitting procedure for chaotic time series,” *Applied Mathematics and Computation*, vol. 95, no. 2-3, pp. 219–243, 1998.

[15] J. A. Domaradzki, K. C. Loh, and P. P. Yee, “Large eddy simulations using the subgrid-scale estimation model and truncated Navier–Stokes dynamics,” *Theoretical and Computational Fluid Dynamics*, vol. 15, pp. 421–450, 2002.

[16] K. Fukami, K. Fukagata, and K. Taira, “Super-resolution analysis via machine learning: a survey for fluid flows,” *Theoretical and Computational Fluid Dynamics*, 2023.

[17] H. Kim, J. Kim, S. Won, and C. Lee, “Unsupervised deep learning for super-resolution reconstruction of turbulence,” *Journal of Fluid Mechanics*, vol. 910, 2021.

[18] R. Vinuesa and S. L. Brunton, “The potential of machine learning to enhance computational fluid dynamics,” *arXiv:2110.02085*, 2021.

[19] M. Ihme, W. T. Chung, and A. A. Mishra, “Combustion machine learning: Principles, progress and prospects,” *Progress in Energy and Combustion Science*, vol. 91, p. 101010, 2022.

[20] L. Nista, H. Pitsch, C. D. K. Schumann, M. Bode, T. Grenga, J. F. MacArt, and A. Attili, “Influence of adversarial training on super-resolution turbulence reconstruction,” *Physical Review Fluids*, vol. 9, p. 064601, Jun 2024.

[21] L. von Rueden, S. Mayer, R. Sifa, C. Bauckhage, and J. Gärcke, “Combining machine learning and simulation to a hybrid modelling approach: Current and future directions,” in *Advances in Intelligent Data Analysis XVIII*, M. R. Berthold, A. Feelders, and G. Krempl, Eds. Cham: Springer International Publishing, 2020, pp. 548–560.

[22] L. Nista, C. D. Schumann, P. Petkov, V. Pavlov, T. Grenga, J. F. MacArt, A. Attili, S. Markov, and H. Pitsch, “Parallel implementation and performance of super-resolution generative adversarial network turbulence models for large-eddy simulation,” *Computers & Fluids*, vol. 288, p. 106498, 2025.

[23] D. K. Lilly, “A proposed modification of the germano subgrid-scale closure method,” *Physics of Fluids A: Fluid Dynamics*, vol. 4, no. 3, pp. 633–635, 1992.

[24] Y. Morinishi and O. V. Vasilyev, “A recommended modification to the dynamic two-parameter mixed subgrid scale model for large eddy simulation of wall bounded turbulent flow,” *Physics of Fluids*, vol. 13, no. 11, pp. 3400–3410, 11 2001.

[25] F. Sarghini, U. Piomelli, and E. Balaras, “Scale-similar models for large-eddy simulations,” *Physics of Fluids*, vol. 11, no. 6, pp. 1596–1607, 1999.

[26] O. Desjardins, G. Blanquart, G. Balarac, and H. Pitsch, “High order conservative finite difference scheme for variable density low Mach number turbulent flows,” *Journal of Computational Physics*, vol. 227, 2008.

[27] V. Eswaran and S. B. Pope, “An examination of forcing in direct numerical simulations of turbulence,” *Computers & Fluids*, vol. 16, no. 3, pp. 257–278, 1988.

[28] L. Nista, C. D. K. Schumann, M. Vivenzo, F. Fröde, T. Grenga, J. F. MacArt, A. Attili, and H. Pitsch, “Homogeneous isotropic turbulence database for training super-resolution data-driven turbulence closure models,” <https://doi.org/10.18154/RWTH-2024-03259>, 2024.

[29] I. Goodfellow, J. Pouget-Abadie, M. Mirza, B. Xu, D. Warde-Farley, S. Ozair, A. Courville, and Y. Bengio, “Generative adversarial networks,” *Communications of the ACM*, vol. 63, no. 11, pp. 139–144, 2020.

[30] X. Wang, K. Yu, S. Wu, J. Gu, Y. Liu, C. Dong, Y. Qiao, and C. C. Loy, “ESRGAN: Enhanced super-resolution generative adversarial networks,” in *Proceedings of the European Conference on Computer Vision workshops*. Springer-Verlag, 2018, p. 63–79. [Online]. Available: https://doi.org/10.1007/978-3-030-11021-5_5

[31] C. Ledig, L. Theis, F. Huszár, J. Caballero, A. Cunningham, A. Acosta, A. Aitken, A. Tejani, J. Totz, Z. Wang, and W. Shi, “Photo-realistic single image super-resolution using a generative adversarial network,” in *2017 IEEE Conference on Computer Vision and Pattern Recognition*, 2017, pp. 105–114.

[32] A. Jolicoeur-Martineau, “The relativistic discriminator: a key element missing from standard GAN,” *arXiv preprint arXiv:1807.00734*, 2018.

[33] L. Mescheder, A. Geiger, and S. Nowozin, “Which training methods for GANs do actually converge?” in *Proceedings of the 35th International Conference on Machine Learning*, ser. Proceedings of Machine Learning Research, J. Dy and A. Krause, Eds., vol. 80. Proceedings of Machine Learning Research, 10–15 Jul 2018, pp. 3481–3490.

[34] L. Nista, C. Schumann, T. Grenga, A. N. Karimi, G. Scialabba, M. Bode, A. Attili, and H. Pitsch, “Turbulent mixing predictive model with physics-based generative adversarial network,” in *10th European Combustion Meeting*, 2021, pp. 460–465.

[35] D. P. Kingma and J. Ba, “Adam: A method for stochastic optimization,” 2017. [Online]. Available: <https://arxiv.org/abs/1412.6980>

[36] G. Arumapperuma, N. Sorace, M. Jansen, O. Bladek, L. Nista, S. Sakhare, L. Berger, H. Pitsch, T. Grenga, and A. Attili, “Extrapolation performance of convolutional neural network-based combustion models for large-eddy simulation: Influence of Reynolds number, filter kernel and filter size,” *Flow, Turbulence and Combustion*, pp. 1–30, 2025.

[37] S. Liu, C. Meneveau, and J. Katz, “Experimental study of similarity subgrid-scale models of turbulence in the far-field of a jet,” *Applied Scientific Research*, vol. 54, pp. 177–190, 1995.

[38] F. Orland, L. Nista, N. Kocher, J. Vanvinckenroye, H. Pitsch, and C. Terboven, “Efficient and scalable AIxeleration of reactive CFD solvers coupled with deep learning inference on heterogeneous architectures,” in *Proceedings of the 2025 International Conference on High Performance Computing in Asia-Pacific Region Workshops*, ser. HPC Asia ’25 Workshops. New York, NY, USA: Association for Computing Machinery, 2025, p. 45–57. [Online]. Available: <https://doi.org/10.1145/3703001.3724386>